Collective modes of excitation in ^{64}Cu

A. Saracino,[1,2,*] S. Zhu,[3,†] N. Sensharma,[1,2] A. D. Ayangeakaa,[1,2,‡] R. V. F. Janssens,[1,2] Q. B. Chen,[4] M. P. Carpenter,[5] P. Chowdhury,[6] A. Gade,[7,8] F. G. Kondev,[5] T. M. Kowalewski,[1,2] T. Lauritsen,[5] E. A. McCutchan,[3] and D. Seweryniak[5]

[1]*Department of Physics and Astronomy, University of North Carolina Chapel Hill, North Carolina 27599, USA*
[2]*Triangle Universities Nuclear Laboratory, Duke University, Durham, North Carolina 27708, USA*
[3]*National Nuclear Data Center, Brookhaven National Laboratory, Upton, New York 11973, USA*
[4]*Department of Physics, East China Normal University, Shanghai 200241, China*
[5]*Physics Division, Argonne National Laboratory, Argonne, Illinois 60439, USA*
[6]*Department of Physics, University of Massachusetts, Lowell, Massachusetts 01854, USA*
[7]*Facility for Rare Isotope Beams, Michigan State University, East Lansing, Michigan 48824, USA*
[8]*Department of Physics and Astronomy, Michigan State University, East Lansing, Michigan 48824, USA*

(Received 22 May 2023; revised 22 January 2024; accepted 1 February 2024; published 16 February 2024)

Medium and high-spin level sequences in ^{64}Cu were investigated using the complex ^{26}Mg(^{48}Ca, $\alpha p5n\gamma$) multinucleon transfer reaction. The experiment was performed at the ATLAS accelerator facility at the Argonne National Laboratory using the Gammasphere array and the fragment mass analyzer (FMA). Two high-spin, quasirotational bands consisting of stretched-$E2$ transitions were observed in coincidence with the known low-spin structure for the first time. These bands share remarkable similarities with highly deformed and/or superdeformed bands observed in the $A \approx 60$–70 mass region. In addition, a regular dipole sequence with weak $E2$ crossover transitions was observed. A general discussion of the observed structures, complemented by theoretical calculations carried out within the framework of the adiabatic and configuration-fixed constrained covariant density functional theory and the quantum particle-rotor model, are presented. The results are interpreted in the context of shell-structure evolution and the collectivity in the mass region.

DOI: 10.1103/PhysRevC.109.024319

I. INTRODUCTION

Over the past three decades, the structure of nuclei in the $A = 60$–70 mass region has been extensively scrutinized in a variety of experimental and theoretical investigations. As a result, there is now a wealth of information about the changes in shell structure associated with increasing neutron excess and angular momentum, the corresponding shape/phase transitions and coexistence, as well as the emergence of collective behavior. Specifically, the dominance of single-particle/hole excitations at low spins and the manifestation of well-established collectivity at medium to high spins are established as being among the most dominant characteristics of these nuclei. Some recent examples include the level structures reported in ^{56,58,60,62,64}Cr [1,2], ^{58,59,60,62,64,66,68}Fe [2–6], ^{62,63}Ni [7,8], ^{61,62}Co [9,10], ^{66}Zn [11], and ^{62}Cu [12]. In all these cases, it is shown that particle/hole excitations within the fp shell are responsible for the low-lying level structure. However, as the angular momentum of the system increases, excitations to the shape-driving intruder $g_{9/2}$ orbital become significant, leading to the onset of collectivity.

In addition to collective excitations at "normal" deformation ($\beta_2 \approx 0.2$–0.3), certain nuclei in this region also exhibit superdeformation. This phenomenon was originally predicted in the $A \approx 60$ region based on calculations of large superdeformed shell gaps in the single-particle energy levels, corresponding to deformations, in the range $\beta_2 \approx 0.4$–0.6, for $N, Z \approx 30, 32$ [13]. Indeed, the first observation of a superdeformed band in this region was reported for the ^{62}Zn nucleus [13]. This was followed by similar observations in the neighboring ^{58,59}Cu [14,15] and ^{60,61}Zn [16,17] nuclei. More recently, a high-spin quasirotational band with striking similarities to superdeformed bands in ^{68}Ge [18] was reported in ^{66}Zn [11]. Shell-model calculations, such as those presented in Refs. [16,19], suggest that the excitation of protons and neutrons from the $f_{7/2}$ shell into the intruder $g_{9/2}$ shell is responsible for the emergence of these superdeformed structures. Using the configuration-dependent, shell-correction approach with the cranked Nilsson potential [20,21], the work of Ref. [13] confirmed the above shell-model predictions, and determined the configurations of the observed superdeformed bands in ^{62}Zn to be $\nu(f_{7/2})^{-2}(g_{9/2})^{2,3}$. Moreover, comparisons of the experimental dynamic moments of inertia, $\mathcal{J}^2$, for various superdeformed bands in this region have revealed that the quadrupole deformation of these bands increases with the number of particles occupying the $g_{9/2}$ shell [22]. Therefore, in addition to facilitating comparisons between

*asaracino@unc.edu
†Deceased.
‡ayangeak@unc.edu

 ©2024 American Physical Society

results from shell-model calculations and mean-field cranking models, the $A \approx 60$ nuclei, with $N \approx Z$ and minimal valence particles/holes above the Fermi surface provide a special avenue for the investigation of superdeformed structures.

In the present work, a detailed study of the level structure of the ^{64}Cu nucleus was undertaken following an experiment performed at Argonne National Laboratory. Using the ^{26}Mg(^{48}Ca, $\alpha p5n\gamma$) complex multinucleon transfer reaction, a significantly modified and substantially extended level scheme of ^{64}Cu is proposed up to $I^{\pi} = 29^{-}$. Some of the earliest works on this nucleus can be found in Refs. [23–29], where energy levels up to $E_x = 3.99$ MeV were excited. Due to experimental limitations, firm spin and parity assignments were only possible for states below 1 MeV [24]. More recently, a high-statistics measurement was performed for ^{64}Cu using the ^{59}Co(^{7}Li, pn)^{64}Cu heavy-ion fusion evaporation reaction [30], and states up to $E_x \approx 6$ MeV and $I^{\pi} \approx 10\hbar$ were reported. The proposed level scheme (of Ref. [30]) consisted mostly of low-lying states of dominant single-particle character. The present work has found significant disagreements with this scheme. Based on triple-γ coincidence measurements, the placement of several γ-ray transitions has been revised. High-statistics angular distributions have also enabled firm spin assignments for states where those were only tentatively proposed previously. In addition, utilizing the highly-sensitive Gammasphere array [31], coupled with the Fragment Mass Analyzer (FMA) [32], the present work has also identified three rotational-like sequences at medium and high spins; one dipole band comprising strong $\Delta I = 1$ transitions and two rotational cascades with strong $\Delta I = 2$ γ rays. These bands were all observed to be in coincidence with the low-lying structure. A comparison with neighboring nuclei has revealed that the two $\Delta I = 2$ bands exhibit properties similar to those of superdeformed bands found in the region. These two new sequences were investigated further with theoretical calculations within the framework of the adiabatic and configuration-fixed constrained covariant density functional theory, and the quantum particle-rotor model.

The paper is organized as follows: Section II describes the experimental technique, including the reaction mechanism, the setup employed, and the method for assigning quantum numbers. Details about the present level scheme and a discussion of the differences with previous works are given in Sec. III. The newly observed structures are discussed extensively in Sec. IV, along with results of theoretical calculations carried out within the framework of the adiabatic and configuration-fixed constrained covariant density functional theory and the quantum particle rotor model. These provide microscopic insight into the nature of the observed excitations. Conclusions are presented in Sec. V.

II. EXPERIMENT

The experiment was performed at the ATLAS superconducting linear accelerator at Argonne National Laboratory. Most of the relevant information about the experimental setup and conditions has been published previously and, as a result, the experimental procedure and analysis methods are only briefly summarized here. Interested readers are referred to Refs. [7–9] for more details. In the present study, medium- and high-spin states in ^{64}Cu were populated in the $\alpha p5n\gamma$ channel of the inverse-kinematic, multinucleon transfer reaction between a ^{48}Ca beam and ^{26}Mg target. Three beam energies of 275, 290, and 320 MeV were used to bombard a 0.97-mg/cm^2-thick, self-supporting, isotopically enriched, ^{26}Mg target. These energies were chosen to be roughly 200% above the Coulomb barrier in order to enhance the multinucleon transfer processes. Prompt γ rays emitted in the deexcitation process were detected with Gammasphere, a 4π array of 101 Compton-suppressed high-purity germanium (HPGe) detectors. For isotopic identification, the recoiling products were separated according to their mass-to-charge (m/q) ratio by the Fragment Mass Analyzer (FMA). A microchannel plate (MCP) detector placed at the FMA focal plane was used to determine the position and time of flight of the reaction residues, while a threefold segmented ionization chamber, located behind the focal plane, measured the energy loss. The recoils were detected in kinematic coincidence ($\Delta T = 50$ ns) with two or more γ rays and were recorded event by event. After Doppler correction, γ-ray events associated with the decay of ^{64}Cu recoils were sorted into a fully symmetrized, two-dimensional ($E_\gamma - E_\gamma$) coincidence matrix while those arising from all Cu ions populated in the reaction were sorted into a three-dimensional ($E_\gamma - E_\gamma - E_\gamma$) cube. These were analyzed using the RADWARE suite of codes [33].

Spin quantum numbers for newly identified and previously known transitions were assigned by examining the observed decay patterns together with high-statistics angular distribution and angular correlation data. The angular distribution analysis was performed using coincidence matrices sorted such that energies of γ rays detected at specific Gammasphere angles (measured with respect to the beam direction) $E_\gamma(\theta)$, were incremented on one axis, while the energies of coincident γ rays detected at any angle, E_γ(any), were placed on the other. To improve statistics, adjacent rings of Gammasphere, and those corresponding to angles symmetric with respect to 90° in the forward and backward hemispheres, were combined. In this way, a total of eight matrices were created, with the angles 17.2°, 34.2°, 37.2°, 50.2°, 58.2°, 69.2°, 79.2°, and 90.2°. By gating on the E_γ(any) axis and projecting on the $E_\gamma(\theta)$ one, background-subtracted and efficiency-corrected spectra were generated. From these, the intensities of transitions of interest were extracted and fitted to the angular distribution function $W(\theta) = 1 + A_2P_2(\cos\theta) + A_4P_4(\cos\theta)$, where P_2 and P_4 are the Legendre polynomials. The coefficients A_2 and A_4, containing the information about the multipolarity of the transitions, were obtained with an angular distribution code which uses the Markov Chain Monte Carlo (MCMC) high-dimensional probability sampling technique [34]. Figure 1 compares sample angular distributions with fits obtained with this code for some ^{64}Cu transitions of interest.

For transitions where a complete angular distribution analysis was not possible due to low statistics, a two-point angular correlation ratio, R_{ac}, proved useful. This defines a normalized ratio of γ-ray intensities observed at forward (f) and/or backward (b) angles to those observed in detectors centered around 90° with respect to the beam direction. For this purpose, three coincidence matrices were created

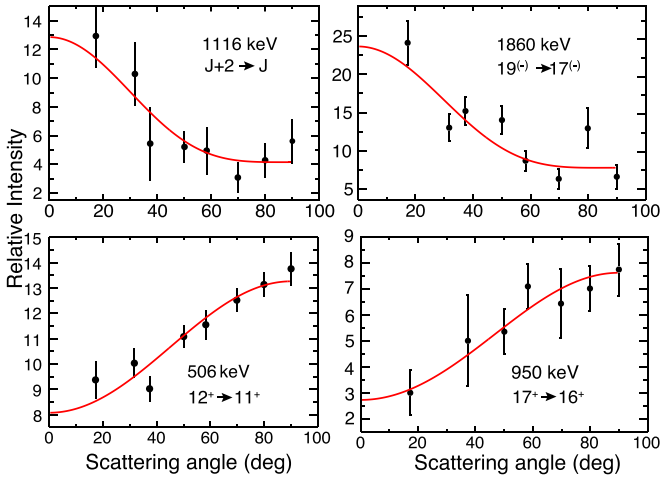

FIG. 1. Angular distributions for some relevant ^{64}Cu transitions. Experimental data are shown as black circles, while the angular-distribution fits correspond to the red curve.

corresponding to γ rays detected at forward (31.2°, 37.2°, 50.2°), backward (129.2°, 142.2°, 148.2°, 162.2°), and central (69.2°, 79.2°, 80.2°, 90.2°, 99.2°, 100.2°, 110.2°) angles on one axis, and γ rays detected at all these angles grouped on the other. Gating on the all-angle axis, the intensity of the coincident γ rays was obtained and the ratio $R_{\rm ac} = I^{\gamma_2}_{\rm forward/backward}({\rm Gate}^{\gamma_1}_{{\rm all}\theta})/I^{\gamma_2}_{\rm middle}({\rm Gate}^{\gamma_1}_{{\rm all}\theta})$ calculated. Here, γ_1 and γ_2 are two successive γ rays and θ is the angle with respect to the beam direction. This ratio, which is independent of the multipolarity of the gating transition, was established to be greater than or equal to ≈1.2 for stretched-quadrupole transitions and less than or equal to ≈0.9 for stretched-dipole ones. Table I presents the extracted A_2 and A_4 coefficients, the $R_{\rm ac}$ ratios, and the adopted multipolarities for all the transitions observed in the present work.

Furthermore, following a procedure similar to that presented in Ref. [8], the Doppler-shift attenuation method (DSAM) was used to estimate a transition quadrupole moment, Q_t, for the rotational band labeled as Band 1 hereafter. The measurement was carried out using the $E_{\rm beam} = 320$ MeV data, which enabled the extraction of fractional Doppler shifts $F(\tau)$ and associated errors for some of the more strongly populated states within the band. Gamma rays emitted from these states were corrected with a Doppler shift factor corresponding to the initial velocity β_0 of the recoiling ions. The resulting Doppler-corrected data were sorted into seven matrices with the condition that γ rays detected at specific angles (17.3°, 35.6°, 50.1°, 58.3°, 69.8°, 80.0°, and 90.0°) on one axis must be in coincidence with those detected at any angle on the other. The peak centroids for each angle were found to be slightly shifted, showing that the transitions were emitted while the recoiling ions slowed down in the ^{26}Mg target. The average instantaneous recoil velocity β_t for each transition was then calculated using linear fits of the energy changes as a function of detector angle θ, and the fractional Doppler shift $F(\tau) = \beta_t/\beta_0$ was extracted. A plot of the extracted $F(\tau)$ values as a function of transition energy is presented in Fig. 2. The transition quadrupole moment, Q_t, was obtained by comparing the experimental $F(\tau)$ values to those computed using the Monte Carlo simulation code WLIFE4 [35], with the stopping powers provided by the SRIM-2010 package [36]. The following usual assumptions were employed in order to calculate the Q_t value using this method [8]: (i) all levels in Band 1 were assumed to have the same Q_t moment, (ii) side-feeding into each level was assumed to have the same quadrupole moment, $Q_{\rm sf}$ and the same dynamic moment of inertia as the main band into which it feeds, and (iii) throughout the analysis, a parameter $T_{\rm sf}$ was set to $T_{\rm sf} = 1$ fs to account for a one-step side-feeding delay on top of the band. A χ^2 minimization with the parameters Q_t and $Q_{\rm sf}$ was performed for the experimental $F(\tau)$ values. The best fit to the data is indicated by the dashed red line in Fig. 2. An additional ≈15% systematic error was added to the final result to take into account the uncertainties associated with the simulation of the stopping process, and the assumptions listed above.

III. LEVEL SCHEME

The level scheme of ^{64}Cu established in the present work is displayed in Figs. 3 and 4. This was developed primarily using a combination of energy sums, intensity balances and $\gamma - \gamma$ coincidence relationships. It was cross-checked, for the most intense transitions, with the $\gamma - \gamma - \gamma$ coincidence cube constructed from all Cu events (see Sec. II). Spins were assigned based on angular distributions and correlation ratios, while parity assignments for low-lying states followed those of previous work. For newly established, higher-lying states, it was assumed that the transitions linked levels with the same parity. The assigned transitions and their properties are summarized in Table I. Overall, the level scheme from the present work combines three main structures: a low-spin one comprising mostly single-particle excitations, a dipole band with weak $E2$ crossover transitions at medium spins, and two high-spin rotational sequences composed of stretched-$E2$ transitions. Combined, this represents a significant extension of the level scheme compared to that proposed by Samanta *et al.*, in Ref. [30].

The background-subtracted and efficiency-corrected total projection obtained from the ^{64}Cu coincidence matrix is displayed in Fig. 5. This spectrum highlights some of the dominant transitions. For example, the 159-, 203-, 212-, and 314-keV γ rays (marked in black) belonging to the low-spin region are clearly visible. Also visible is the 412-keV peak (red in Fig. 5) depopulating the bandhead of the newly established dipole sequence (labeled as Band 3 in Fig. 3). Other transitions within Band 3 (viz., 459, 506, and 577 keV) are indicated as well. Peaks marked in blue and green correspond to the newly identified transitions constituting Bands 1 and 2, respectively. The detailed structure and nature of these bands are discussed in Sec. IV.

Most of the transitions observed within the low-spin structure are largely in agreement with those observed in earlier works [23–25,30], except for a few discrepancies. One of these is the placement of the 314 − 479-keV pair of transitions. Ref. [30] reports three different γ rays in the low-spin region, each with an energy of 314 keV which appear in coincidence with four different 479-keV transitions: 479 → 314

TABLE I. γ-ray energies, relative intensities, energy of the initial state, initial and final spins, angular correlation ratios (R_{ac}), experimental angular distribution coefficients (A_2), and assigned multipolarities for the transitions shown in Figs. 3 and 4. Multipolarities marked with asterisks are consistent with assignments previously reported in Ref. [30]. The relative intensities (I_γ) of the γ-ray transitions were determined with gates on the 159- and 278-keV transitions. All transitions with energies enclosed in parentheses are uncertain.

E_γ (keV)	I_γ	E_i (keV)	$I_i^\pi \rightarrow I_f^\pi$	R_{ac}	A_2	Mult.
84.45(14)	0.09(1)	361.7(3)	$3^+ \rightarrow 2^+$	0.30(18)	−0.52(23)	$M1+E2$
119.1(4)	0.99(10)	277.94(2)	$2^+ \rightarrow 2^+$			
137.36(8)		745.58(9)	$3^+ \rightarrow 2^+$			
159.03(2)		159.03(2)	$2^+ \rightarrow 1^+$	0.85(1)	−0.14(7)	$M1(+E2)^*$
198.5(1)		2272.9(8)	$6^- \rightarrow 5^-$	0.84(1)	−0.30(2)	$M1+E2$
202.62(5)	49.1(5)	361.7(3)	$3^+ \rightarrow 2^+$	0.83(1)		$M1+E2^*$
211.89(2)	29.79(5)	573.5(3)	$4^+ \rightarrow 3^+$	0.85(1)		$M1+E2^*$
228.51(7)	8.4(8)	2811.8(8)	$6^- \rightarrow (5)^+$	0.86(6)	−0.242(85)	$E1$
249.79(3)	3.89(39)	3126.7(8)	$7^- \rightarrow 7^+$	0.85(6)	0.117(32)	$E1$
277.94(2)		277.94(2)	$2^+ \rightarrow 1^+$	0.86(14)		$M1+E2^*$
300.95(24)	0.78(8)	4569.6(2)	$10^- \rightarrow 9^-$	0.78(9)	−0.13(14)	$M1+E2$
313.70(4)	20.56(41)	3126.7(8)	$7^- \rightarrow 6^-$	0.83(2)	−0.296(21)	$D+Q^*$
320.63(6)	1.49(15)	894.66(36)	$3^+ \rightarrow 4^+$	0.9(1)		$D+Q^*$
369.3(6)	0.51(5)	2074.0(7)	$5^- \rightarrow 4^+$	0.98(12)	−0.247(53)	$E1$
383.8(2)	2.0(2)	745.58(9)	$3^+ \rightarrow 3^+$	0.88(5)	−0.125(69)	D^*
402.9(5)	0.31(3)	4569.6(2)	$10^- \rightarrow 9^-$	0.84(8)	−0.25(11)	$M1+E2$
412.49(4)	6.7(7)	5378.23(30)	$10^+ \rightarrow 9^+$	0.80(5)	−0.245(82)	$M1+E2$
414.0(3)	1.9(2)	775.7(6)	$4^+ \rightarrow 3^+$	0.86(2)	−0.317(27)	$M1+E2$
426.91(4)	2.17(22)	2517.57(60)	$5^- \rightarrow 4^-$	0.72(12)		$D+Q^*$
435.2(9)	2.13(21)	2811.8(8)	$6^- \rightarrow 7^-$	0.86(2)	−0.34(15)	$M1+E2^*$
459.14(06)	10.75(108)	5837.72(7)	$11^+ \rightarrow 10^+$	0.85(2)	−0.252(25)	$M1+E2$
467.92(9)	30.2(302)	745.58(9)	$3^+ \rightarrow 2^+$	0.77(2)	−0.325(27)	$M1+E2^*$
479.20(6)	19.4(19)	3605.4(8)	$8^- \rightarrow 7^-$	0.84(1)	−0.232(10)	$M1+E2$
481.42(10)		2074.0(7)	$5^- \rightarrow 6^-$	0.87(2)	−0.235(22)	$M1+E2$
496.3(3)	1.35(14)	6334.0(3)	$12^+ \rightarrow 11^+$	0.70(3)	−0.428(43)	$M1+E2$
498.6(3)		2876.94(178)	$7^+ \rightarrow 7^-$	0.78(5)	0.106(43)	$E1$
506.39(4)	6.43(64)	6344.11(32)	$12^+ \rightarrow 11^+$	0.79(3)	−0.283(37)	$M1+E2$
522.3(4)	0.30(3)	4917.6(6)	$10^- \rightarrow 9^-$	0.72(5)	−0.66(8)	$M1+E2$
539.89(21)	0.20(2)	2811.8(8)	$6^- \rightarrow 6^-$	0.92(3)	−0.082(101)	$M1+E2^*$
561.3(4)	4.33(43)	4166.17(40)	$9^- \rightarrow 8^-$	0.96(2)	−0.183(27)	$M1+E2$
565.00(3)		1459.5(4)	$4^- \rightarrow 3^+$	0.87(3)	−0.31(52)	$D+Q^*$
568.2(2)		2272.9(8)	$6^- \rightarrow 4^+$	1.09(5)	−0.04(5)	$M2$
576.7(5)	26.6(27)	6920.29(50)	$13^+ \rightarrow 12^+$	0.93(2)	−0.119(41)	$M1+E2$
578.55(18)	6.89(69)	6313.38(30)	$12^- \rightarrow 11^-$	1.16(4)	0.324(6)	$E2$
579.20(12)	2.27(23)	5378.23(22)	$10^+ \rightarrow 8^+$	1.22(8)	0.251(32)	$E2$
586.01(17)	2.14(21)	6920.29(50)	$13^+ \rightarrow 12^+$	0.9(1)	−0.32(14)	$M1+E2$
603.8(1)		2876.94(178)	$7^+ \rightarrow 6^-$	0.90(6)	−0.947(55)	$E1$
608.5(4)	1.13(11)	608.5(4)	$2^+ \rightarrow 1^+$	0.70(7)	−0.645(75)	$M1+E2$
609.3(1)		3800.7(6)	$9^- \rightarrow 8^-$	0.76(5)	−0.438(35)	$M1+E2^*$
612.72(12)	0.93(9)	5529.15(94)	$11^- \rightarrow 10^-$	0.85(6)	−0.422(63)	$M1+E2$
617.0(6)	9.80(98)	894.66(36)	$3^+ \rightarrow 2^+$	0.61(3)	−0.601(61)	$M1+E2^*$
630.0(6)	1.71(17)	2090.66(92)	$4^- \rightarrow 4^-$	0.95(6)	0.87(14)	$D+Q^*$
647.54(7)	0.51(5)	4917.6(6)	$10^- \rightarrow 9^-$	1.03(8)	−0.325(73)	$M1+E2$
664.25(2)	6.77(68)	4269.65(84)	$9^- \rightarrow 8^-$	0.87(3)	−0.204(28)	$M1+E2$
679.07(4)	3.68(37)	2272.9(8)	$6^- \rightarrow 6^-$	0.78(4)	−0.341(35)	$M1+E2$
686.83(23)	4.17(42)	7607.12(94)	$14^+ \rightarrow 13^+$	0.77(4)	−0.294(47)	$M1+E2$
730.7(8)	2.49(25)	8336.99(103)	$15^+ \rightarrow 14^+$	0.92(4)		$M1+E2$
737.8(1)	1.0(1)	2811.8(8)	$6^- \rightarrow 5^-$	0.94(4)	−0.29(15)	$M1+E2$
750.3(4)	0.246(24)	4917.6(6)	$10^- \rightarrow 9^-$	0.79(4)	−0.305(57)	$M1+E2$
784.23(9)	4.12(41)	6313.38(30)	$12^- \rightarrow 11^-$	0.82(2)		$M1+E2$
785(2)	4.12(41)	2378.14(206)	$7^- \rightarrow 6^-$	0.88(2)	−0.571(40)	$M1+E2^*$
789.7(8)	3.11(31)	4395.1(8)	$9^- \rightarrow 8^-$	0.86(2)		$M1+E2$
794.98(15)		3312.55(95)	$7^+ \rightarrow 5^-$	1.34(14)		$(M2+E3)$

TABLE I. (*Continued.*)

E_γ (keV)	I_γ	E_i (keV)	$I_i^\pi \rightarrow I_f^\pi$	R_{ac}	A_2	Mult.
813.0(6)	0.78(8)	3191.14(208)	$8^- \rightarrow 7^-$	0.87(7)		$M1+E2^*$
817.20(19)	0.71(7)	5734.56(70)	$11^- \rightarrow 10^-$	0.79(3)	−0.557(50)	$M1+E2$
831.2(1)	0.56(6)	2811.8(8)	$6^- \rightarrow 5^+$	0.71(15)		$E1$
868.7(4)	3.50(35)	9205.12(98)	$16^+ \rightarrow 15^+$	0.67(6)	−0.325(98)	$M1+E2$
879.1(6)	1.53(15)	2583.32(72)	$(5)^+ \rightarrow 4^+$	0.73(8)	−0.206(92)	$M1+E2$
892.0(5)		6811.33(54)	$12^- \rightarrow 11^-$	1.00(56)	−0.312(95)	$M1+E2$
895.34(177)	0.74(7)	2876.94(178)	$7^+ \rightarrow 5^+$	1.55(32)		$E2$
950.38(7)	2.72(27)	10156.07(98)	$17^+ \rightarrow 16^+$	1.05(11)	−0.34(12)	$M1+E2$
958.36(3)	2.74(27)	1704.71(12)	$4^+ \rightarrow 3^+$	1.09(14)	−0.291(41)	$M1+E2^*$
965.3(3)	1.64(16)	6344.11(32)	$12^+ \rightarrow 10^+$	1.16(2)	0.271(65)	$E2$
994.01(14)	0.78(8)	1769.54(40)	$5^+ \rightarrow 4^+$	1.07(10)	−0.56(7)	$M1+E2$
1015.78(20)	1.35(14)	5919.16(63)	$11^- \rightarrow 10^-$	0.64(7)	−0.354(99)	$M1+E2$
1019.6(5)	2.12(21)	1593.14(80)	$6^- \rightarrow 4^+$	1.10(6)	0.264(58)	$M2+E3^*$
1035.3(1)	0.78(8)	11191.87(50)	$18^+ \rightarrow 17^+$	0.76(16)	−0.111(12)	$M1+E2$
1042.6(6)	1.97(20)	2811.8(8)	$6^- \rightarrow 5^+$	0.86(4)	−0.425(54)	$E1$
1055.90(14)	6.95(70)	7867.23(200)	$13^{(-)} \rightarrow 12^-$	0.95(17)		
1082.57(3)	1.15(12)	6920.29(50)	$13^+ \rightarrow 11^+$	1.34(14)	0.06(12)	$E2$
1097.8(7)		1459.5(4)	$4^- \rightarrow 3^+$	0.69(2)	−0.109(55)	$D+Q*$
1102.7(6)	2.14(21)	4903.4(6)	$10^- \rightarrow 9^-$	0.48(3)	−0.824(36)	$M1+E2$
1107.09(81)	7.80(78)	2811.8(8)	$6^- \rightarrow 4^+$	1.08(21)		
1116.15(10)	9.40(94)	x+1116.15(10)	$J+2 \rightarrow J$	1.50(18)	0.85(13)	$E2$
1131.17(11)		1704.71(12)	$4^+ \rightarrow 4^+$	0.67(22)		$M1+E2$
1143.6(6)		2876.94(178)	$7^+ \rightarrow 5^+$	0.81(34)		
1159.3(3)	2.38(24)	1732.84(60)	$5^+ \rightarrow 4^+$	0.68(4)	−0.665(53)	$M1+E2^*$
1164.96(17)	1.55(16)	5734.56(70)	$11^- \rightarrow 10^-$	0.50(11)	0.14(18)	$M1+E2$
1194.0(7)	0.51(5)	2090.66(92)	$4^- \rightarrow 3^+$	0.65(4)	−0.504(53)	$D+Q^*$
1196.0(4)	1.43(14)	1769.54(40)	$5^+ \rightarrow 4^+$	0.94(10)	−0.501(54)	$M1+E2$
1219.4(1)	0.40(04)	2811.8(8)	$6^- \rightarrow 6^-$	0.72(22)		$M1+E2^*$
1259.5(1)	0.70(7)	5529.15(94)	$11^- \rightarrow 9^-$	1.47(29)	0.29(21)	$E2$
1263.0(9)		7607.12(94)	$14^+ \rightarrow 12^+$	1.79(40)	0.6(2)	$E2$
1283.8(9)		2876.94(30)	$7^+ \rightarrow 6^-$	0.68(36)		
1312.2(15)	1.68(17)	4917.6(6)	$10^- \rightarrow 8^-$	1.18(6)	0.058(52)	$E2$
1361.70(23)		5529.15(94)	$11^- \rightarrow 9^-$	1.19(22)	0.2(3)	$E2$
1387.09(9)		x+2503.24	$\mathrm{J}+4 \rightarrow \mathrm{J}+2$	1.18(32)	0.423(13)	$E2$
1389.29(8)	2.14(21)	9256.6(7)	$15^{(-)} \rightarrow 13^{(-)}$	1.43(8)	0.24(11)	$E2$
1408.0(7)	1.47(15)	1769.54(40)	$5^+ \rightarrow 3^+$	1.04(11)		
1415.36(22)	1.36(14)	7759.0(24)	$14^+ \rightarrow 12^+$	1.60(34)	0.82(16)	$E2$
1416.7(9)		8336.99(103)	$15^+ \rightarrow 13^+$	1.77(90)	0.236(11)	$E2$
1424.98(11)	1.77(18)	7759.0(2)	$14^+ \rightarrow 12^+$	1.00(33)		
1465.3(7)	0.98(10)	5734.56(70)	$11^- \rightarrow 9^-$			
1497.6(7)	0.69(7)	9256.6(7)	$15^{(-)} \rightarrow 14^+$	0.99(17)	−0.01(33)	$E1$
1516.4(2)	1.71(17)	2090.66(92)	$4^- \rightarrow 4^+$	0.82(33)	0.78(35)	$D+Q^*$
(1522(2))	0.67(7)	7867.23(200)	$13^{(-)} \rightarrow 12^+$	0.82(31)	−0.241(55)	$(E1)$
(1532.0(6))	0.45(5)	7867.23(200)	$13^{(-)} \rightarrow 12^+$	1.04(10)	0.03(20)	$(E1)$
1579.4(9)		3312.55(95)	$7^+ \rightarrow 5^+$	1.44(14)	0.38(9)	$E2$
1598(2)	0.27(3)	3191.14(208)	$8^- \rightarrow 6^-$	1.17(7)	0.397(96)	$E2+M3^*$
1598.24(5)		9205.12(98)	$16^+ \rightarrow 14^+$	1.45(21)	0.47(16)	$E2$
1619.9(2)	1.94(19)	1981.6(5)	$5^+ \rightarrow 3^+$	1.12(6)	0.153(63)	$E2$
1624.38(7)	0.60(06)	10880.9(7)	$17^{(-)} \rightarrow 15^{(-)}$	1.07(6)	0.068(65)	$E2$
1635.91(15)	3.77(38)	x+4139.15	$J+6 \rightarrow J+4$	1.15(24)	1.126(57)	$E2$
1653.5(3)	0.44(4)	4965.74(95)	$9^+ \rightarrow 7^+$	1.19(8)		$E2$
1680.54(18)	0.95(10)	2254.08(48)	$6^+ \rightarrow 4^+$	1.30(13)	0.05(12)	$E2$
1787.0(5)	0.402(40)	12978.32(58)	$19^+ \rightarrow 18^+$	0.60(15)	−0.154(295)	$M1+E2$
(1818.0(4))	0.169(17)	10156.07(98)	$17^+ \rightarrow 15^+$	1.25(61)		
1860.49(9)	1.2(2)	12741.39(11)	$19^{(-)} \rightarrow 17^{(-)}$	1.21(7)	0.054(63)	$E2$
1916.31(10)	0.106(10)	x+6055.46	$J+8 \rightarrow J+6$	1.28(32)	0.23(11)	$E2$

TABLE I. (*Continued.*)

E_γ (keV)	I_γ	E_i (keV)	$I_i^\pi \rightarrow I_f^\pi$	R_{ac}	A_2	Mult.
1947.53(14)		7867.23(200)	$13^{(-)} \rightarrow 11^-$	1.29(65)	0.47(21)	$E2$
1986.0(3)		11191.87(50)	$18^+ \rightarrow 16^+$			
2010.4(3)	1.11(11)	2583.32(72)	$(5)^+ \rightarrow 4^+$			
2115.72(11)	1.32(13)	14857.11(14)	$21^{(-)} \rightarrow 19^{(-)}$	1.07(6)	0.041(67)	$E2$
2118.65(4)	1.73(13)	5919.16(63)	$11^- \rightarrow 9^-$	1.86(19)	0.620(184)	$E2$
2216.12(12)		x+8271.58	$J+10 \rightarrow J+8$	1.4(14)	0.13(38)	$(E2)$
2422.90(10)	0.999(99)	17280.01(15)	$23^{(-)} \rightarrow 21^{(-)}$	1.59(14)	0.36(10)	$E2$
2545.3(7)	0.15(04)	4799.38(72)	$8^+ \rightarrow 6^+$	1.01(86)	0.89(30)	$E2$
2557.6(3)	0.32(3)	x+10829.18	$J+12 \rightarrow J+10$	1.62(79)	0.18(16)	$(E2)$
2762.35(17)	0.54(5)	20042.36(20)	$25^{(-)} \rightarrow 23^{(-)}$	1.47(18)	0.40(15)	$E2$
2965.9(6)	0.062(6)	x+13795.08	$J+14 \rightarrow J+12$	1.12(59)	0.10(42)	$(E2)$
3108.4(4)	0.10(1)	23150.76(43)	$27^{(-)} \rightarrow 25^{(-)}$	1.41(35)	0.46(41)	$E2$
3415.1(7)		x+17210.18	$J+16 \rightarrow J+14$	1.47(71)	0.26(54)	$(E2)$
3527.7(8)	0.018(002)	26678.46(90)	$29^{(-)} \rightarrow 27^{(-)}$			$(E2)$

keV ($7^- \rightarrow 7^- \rightarrow 6^-$), 314 → 479 keV ($6^- \rightarrow 5^- \rightarrow 6^-$), and 479 → 314 keV ($5^+ \rightarrow 4^+ \rightarrow 4^+$). In the present work, only one instance of a 314-keV γ ray depopulating the 7^- state at 3127 keV and feeding into the 6^- level at 2812 keV is established. In turn, the 7^-, 3127-keV level is fed by a 479-keV γ ray of dipole character de-exciting a 8^- state at 3605 keV. This cascade is likely the same as the 479 → 314 keV ($7^- \rightarrow 7^- \rightarrow 6^-$) sequence reported in Ref. [30] which feeds the level depopulated by the 1041- and 1196-keV γ rays. Another discrepancy is the placement of the 562-keV transition, which was previously reported in Ref. [30] as a quadrupole and placed as depopulating the 9^- state and feeding into the 7^- 3603.9-keV level, which then bifurcated into two branches: The 229–878–479–314–959-keV sequence feeding into the 745.6-keV level and the 479–314–1041–1196-keV cascade. In the present work, the 561-keV γ ray is established to feed primarily the 8^- level depopulated by the 479-keV γ ray, followed sequentially by either the 314 → 1043 → 1196-keV cascade or the 229 → 879 → 958-keV one. Both sequences then feed into the same cluster of states established previously [30]. Figures 7(a) and 7(b) provide coincidence spectra obtained from double gates on the 314- and 479-keV transitions as well as the 479- and 481-keV ones, respectively. These spectra confirm the present reconfiguration of the level scheme and account for almost all the coincidence patterns proposed in Ref. [30]. They also resolve some of the inconsistencies in the previous level scheme. For instance, Fig. 7(b), obtained from double gates on the 479- and 481-keV transitions, shows coincident relationships with the 250- and 1620-keV γ rays, which are not compatible with the level scheme of Ref. [30]. This is more evident in Fig. 8 where a double gate on the 250- and 479-keV transitions reveals coincidence with the 1620- (likely 1617 keV in Ref. [30]) and 896-keV γ rays.

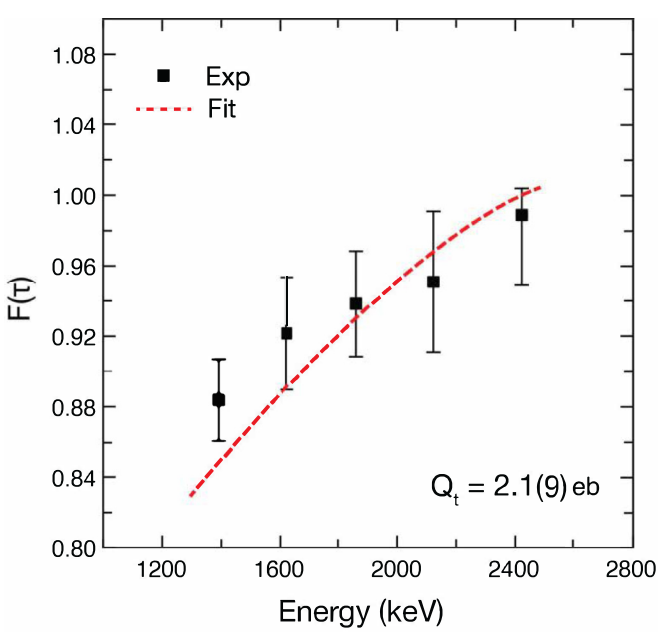

FIG. 2. Experimental (points) and calculated (dashed line) values of the fractional Doppler shift $F(\tau)$ as a function of E_γ for Band 1 in ^{64}Cu. The best fit is represented by the dashed-red line.

As another illustration, the placement of the 369- and 568-keV transitions in the low-spin structure can be clarified by examining the coincidence spectra given in Fig. 9. In Fig. 9(a), a gate on the 369- and 540-keV transitions reveals the presence of the 199-keV γ ray, but not the 568-keV one. In Fig. 9(b), a gate on the 278- and 540-keV transitions shows both the 369- and 568-keV γ rays. In Fig. 9(c), a gate on the 199- and 540-keV lines shows only the 369-keV γ ray, but not the 568-keV one. These results support the new placement proposed in this work. Additionally, Fig. 10 displays the coincidence spectrum obtained by gating on the 790- and 817-keV transitions. The observation of the 579-keV γ ray indicates that it belongs to the same cascade as the gating transitions, which is further evidence for the new placement in this work. It is instructive to note that, while the parity assignments remain unchanged, the spin of these states and many others have been changed based on the results of the present angular distribution and correlation ratio, R_{ac}, analyses. For instance, the 561-keV γ is reassigned a dipole character and connects

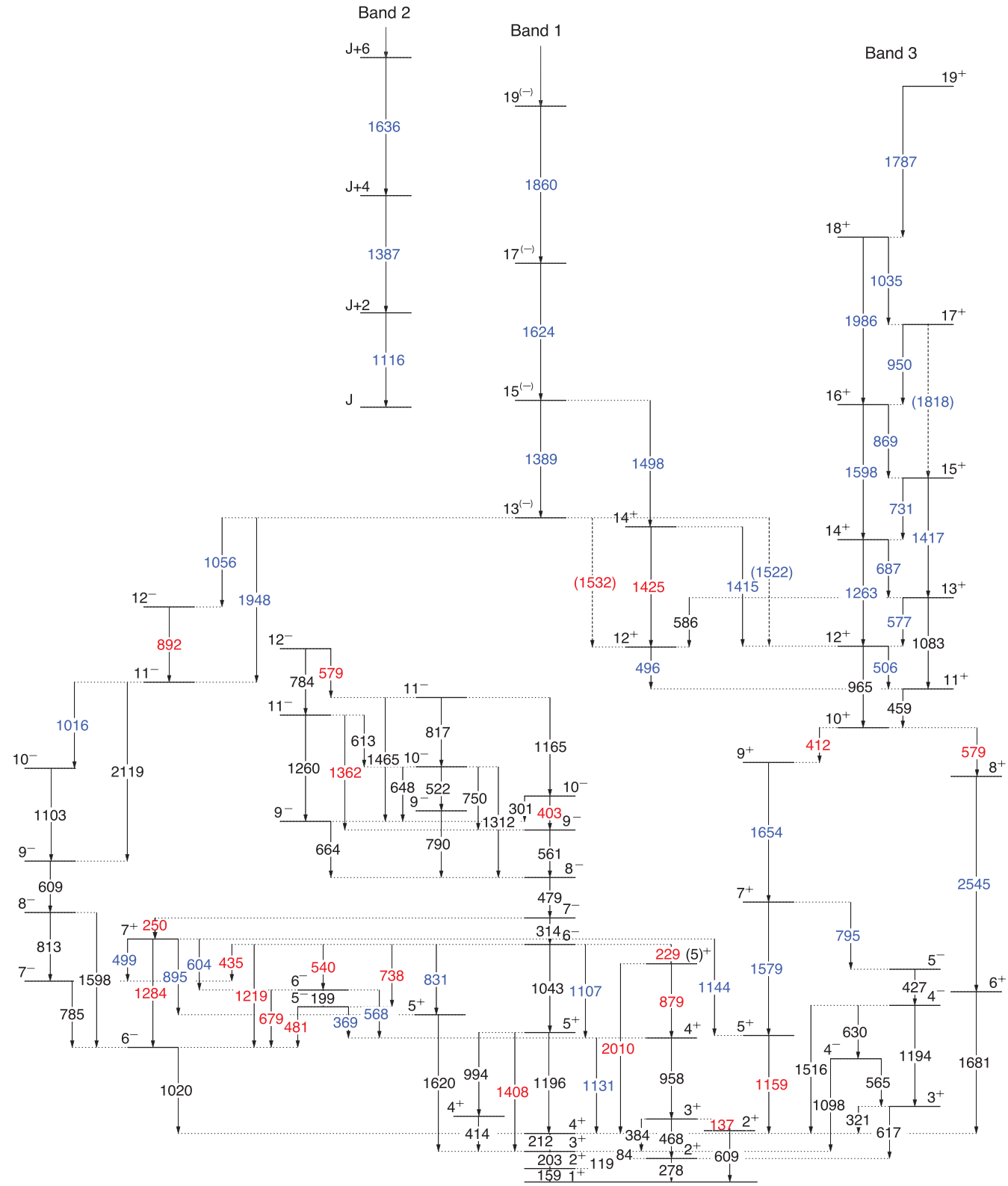

FIG. 3. Lower part of the partial level scheme of ^{64}Cu as observed in the present study. Newly placed transitions are indicated in blue while those that have been reassigned from previous work are given in red. Black-colored transitions are previously known transitions that have been confirmed in the present work. Details of the spin-parity assignments for earlier-known, reassigned, and new transitions are provided in the text and in Table I. Although Band 1 is firmly connected to the low-spin part of the level scheme, the placement of Band 2 is schematic since the absolute excitation energy, spin, and parity are unknown; see text for further details. Transitions indicated with dashed arrows and enclosed in parentheses are uncertain.

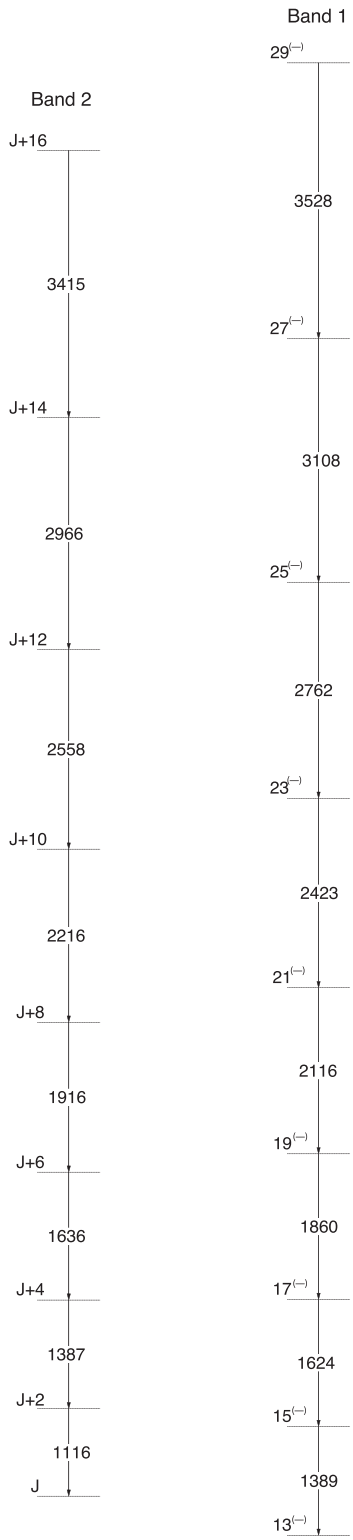

FIG. 4. Continuation of the high-spin part of the level scheme of ^{64}Cu as observed in the present study.

the 9^- and 8^- states. Levels for which the spins are unchanged are indicated by asterisks in Table I.

In addition to the states of predominantly single-particle character observed at low spin, a dipole band (Band 3 in Fig. 3) has also been observed in coincidence with the low-lying structure. This band, comprising the 1787-, 1035-, 950, 869-, 731-, 687-, 577-, 506-, and 459-keV transitions, is built on top of the $I^\pi = 10^+$ bandhead at an excitation energy of 5.4 MeV. It feeds into the low-lying structure via the 412- and 579-keV transitions. A coincidence spectrum obtained by double gating on the 159- and 202-keV γ rays can be found in Fig. 6, where the peaks in red correspond to the Band 3 in-band transitions. Based on angular distribution/correlation analyses, the in-band transitions of Band 3 are predominantly of dipole character. This band was also observed to comprise weak crossover transitions of quadrupole character (1986, 1818, 1598, 1417, 1263, 1083, and 965 keV).

Two rotational sequences, Bands 1 and 2 in Fig. 4, were also populated to high spins and excitation energies. These newly identified bands were found to be composed of regular sequences of $\Delta I = 2$ transitions. Summed coincidence spectra obtained by individually gating on all the in-band transitions of Bands 1 and 2 are presented in Figs. 11(a) and 11(b), respectively. These highlight an almost constant energy spacing between the in-band transitions in both sequences, thereby

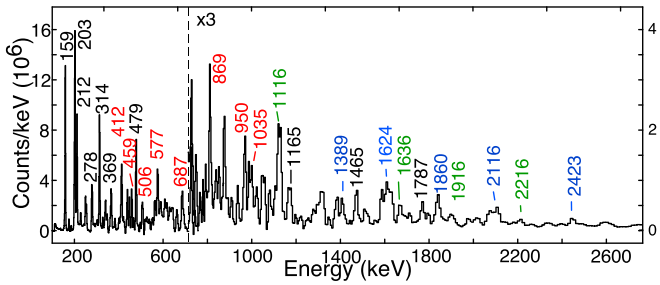

FIG. 5. Background-corrected total projection spectrum obtained from the ^{64}Cu γ-γ-γ coincidence matrix. Transitions within the low-spin region are indicated in black, those within the dipole band are in red, and transitions within rotational Bands 1 and 2 are in blue and green, respectively. The dashed line divides the two regions of the spectrum which correspond to the two different zooms of the y axis: The left axis for the region on the left of the dashed line and the right axis (x3) for the one on the right.

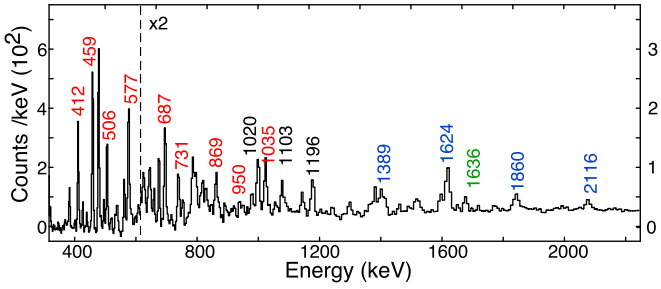

FIG. 6. Coincidence spectrum resulting from a double gate on the 159- and 203-keV. Transitions within the dipole band (labeled in red) and those within rotational Bands 1 and 2 (blue and green, respectively) are indicated. The dashed line divides the two regions of the spectrum which correspond to the two different zooms of the y axis: the left axis for the region on the left of the dashed line and the right axis (x2) for the one on the right.

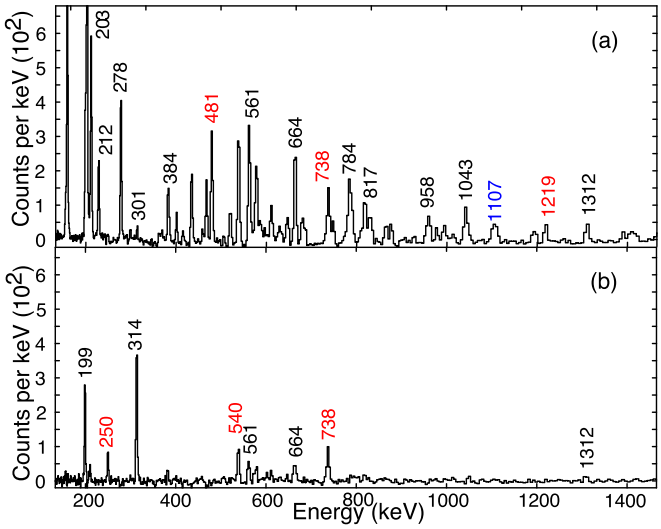

FIG. 7. Coincidence spectra obtained by double gating on (a) the 314- and 479- keV transitions, and (b) the 479- and 481- keV ones. Newly placed transitions are indicated in blue while those that have been reassigned from previous work are given in red. Black-colored γ rays are previously known transitions that have been confirmed in the present work.

suggesting the onset of collectivity. Band 1, built on the $13^{(-)}$ state at an excitation energy of 7.9 MeV, extends up to the $I^{\pi} = 29^{(-)}$ level at 26.7 MeV. It is connected to the lower part of Band 3 via a $\Delta I = 1$, 1522-keV γ ray. Coincidence spectra resulting from a double gate on the in-band 2116- and 2423-keV transitions and that on 1624- and 1860-keV γ rays of Band 1 are displayed in Figs. 13(a) and 13(b), respectively. Coincident γ rays from the low-spin region are marked in black in these figures. For Band 1, the DSAM method was used to determine the transition quadrupole moment. As described above, the extracted experimental fractions of full Doppler shift values $F(\tau)$ were compared with those simulated using the WLIFE4 code, and a transition quadrupole moment of $Q_t = 2.1(9)\,e$b was obtained. Band 2, on the other hand, could not be directly connected to the low-to-medium spin structure of Fig. 3, possibly due to low intensity and fragmented decay paths. Based on information obtained from the FMA, and the

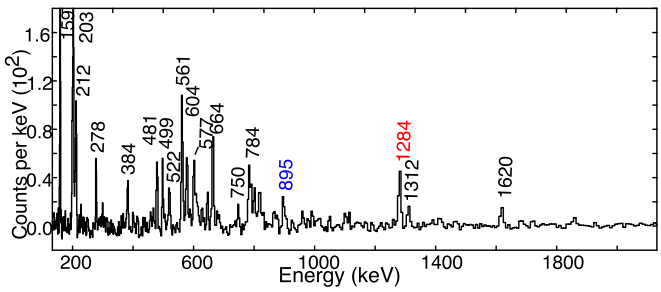

FIG. 8. Coincidence spectrum obtained by double gating on the 250- and 479- keV transitions. Newly placed γ rays are indicated in blue while those that have been reassigned from previous work are given in red. Black-colored γ rays are previously-known transitions that have been confirmed in the present work.

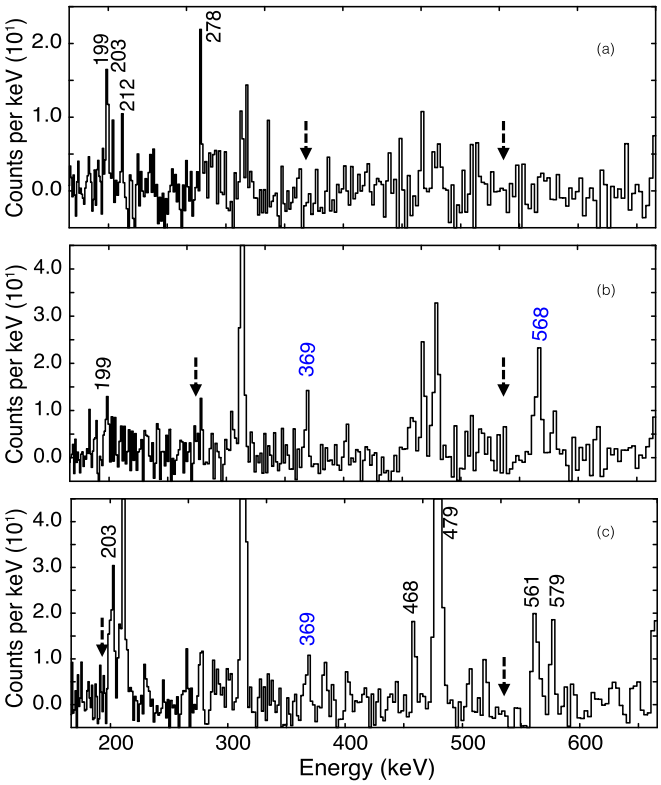

FIG. 9. Coincidence spectra resulting from (a) a double gate on the 369- and 540-keV transitions, (b) a double gate on the 278- and 540-keV ones and (c) a double gate on the 199- and 540-keV lines. Newly-placed transitions are indicated in blue while those that have been reassigned from previous work are given in red. Black-colored transitions are previously known ones that have been confirmed in the present work.

observed coincidence relationships with transitions within the low-lying structure, this band has been firmly assigned to the ^{64}Cu nucleus. Figures 12(a) and 12(b) present coincidence relationships between the in-band transitions of Band 2 and those arising from the low-lying level structure. Angular distribution and correlation analyses have identified the in-band transitions in both Bands 1 and 2 as being of quadrupole character. Some of the relevant angular distributions are presented

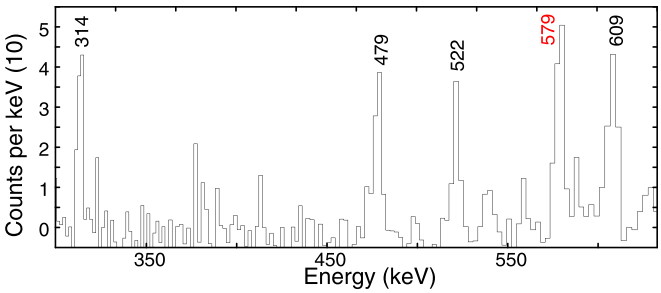

FIG. 10. Coincidence spectrum resulting from a double coincidence gate on 790- and 817-keV transitions. A γ ray reassigned from previous work is given in red. Black-colored transitions are previously known ones that have been confirmed in the present work.

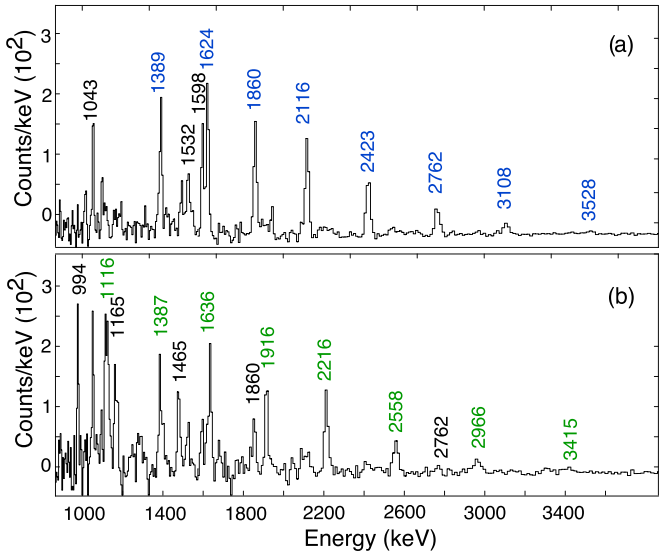

FIG. 11. Coincidence spectra resulting from a gate on the sum of all possible in-band transitions of (a) Band 1 and (b) Band 2. An almost constant energy spacing between the in-band γ-ray transitions in these bands indicates the onset of collectivity.

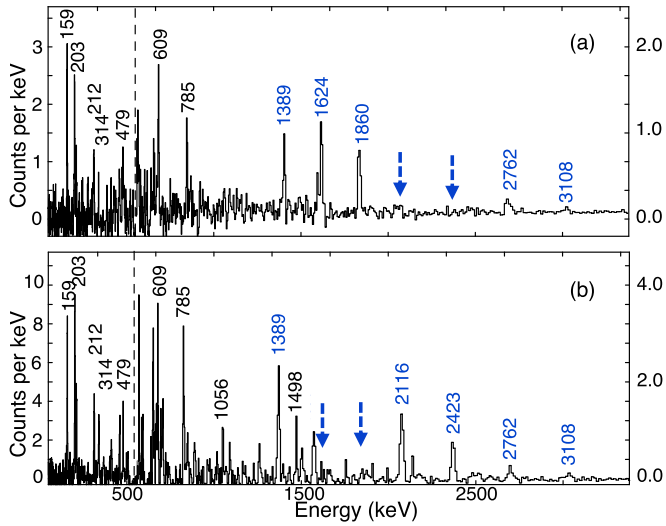

FIG. 13. Coincidence spectra resulting from (a) a double gate on the 2116- and 2423- keV transitions and (b) a double gate on 1624- and 1860-keV ones. Gamma rays from Band 1 (blue) appear in coincidence with those arising from the low-lying level structure (black). The blue arrows point to the gating transitions.

in Fig. 1, and the relevant anisotropy coefficients are listed in Table I. Due to the lack of decay-out transitions, the absolute excitation energies and spins for the levels in this band could not be established.

IV. DISCUSSION

The level structure of the near-magic, odd-odd ^{64}Cu nucleus, albeit more complex, exhibits similarities with those of most other nuclei in the $A \approx 60$ region. In particular, the structure at low spins is dominated by noncollective, single-particle type excitations involving a few valence nucleons. This was recently demonstrated in Ref. [30], where shell-model calculations with the jj44bpn effective interaction indicated that the low-spin, positive-parity states are mostly associated with the $f_{5/2}$, $p_{3/2}$, and $p_{1/2}$ single-particle orbitals. With increasing spin, excitations to the intruder $g_{9/2}$ orbital become significant. Indeed, the observation of collective behavior at high spins in many nuclei of this region has been associated with the increased occupation of the proton and neutron $1g_{9/2}$ orbitals [9–11]. More importantly, particle-hole excitations from the $\pi f_{7/2}$ and $\nu f_{7/2}$ states to the shape-driving $\pi g_{9/2}$ and $\nu g_{9/2}$ orbitals have resulted in the emergence of superdeformed bands in a number of nuclei in this region including ^{56}Ni [37], ^{58,59}Cu [14,15], $^{60-63,65,68}$Zn [16,17,19,38], and ^{68}Ge [18]. In most of these cases, the superdeformed characteristics have been confirmed by lifetime and quadrupole moment measurements. For example, using the fractional Doppler shift method, an average transition quadrupole moment of 2.24(40) eb was extracted for the superdeformed band in ^{59}Cu [15]. For the bands in ^{61}Zn and ^{62}Zn, Q_t values of $3.0^{+0.5}_{-0.4}$ eb ($\beta_2 = 0.50^{+0.07}_{-0.06}$) [17], and $2.7^{+0.7}_{-0.5}$ eb ($\beta_2 = 0.45^{+0.10}_{-0.07}$) [13], respectively, have been reported. In the present study, a transition quadrupole moment of 2.1(9) eb, corresponding to a quadrupole deformation, $\beta_2 = 0.42(14)$, was obtained for Band 1 with the same technique. Collectively, these results support theoretical predictions made with the cranked Nilsson model about the occurrence of high-spin superdeformed bands with deformations of $\beta_2 = 0.41$–0.49 [13] in this region.

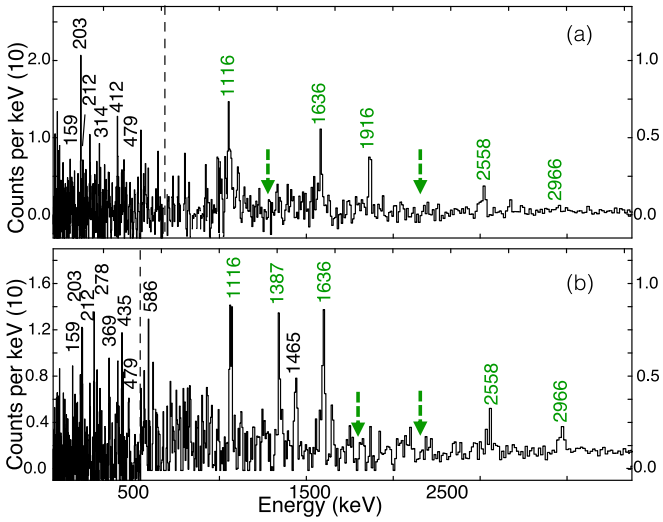

FIG. 12. Coincidence spectra resulting from (a) a double coincidence gate on 2216- and 1387-keV transitions and (b) a double gate on 1916- and 2216-keV ones. Gamma rays from band 2 (green) appear in coincidence with those arising from the low-lying level structure (black). The green arrows point to the gating transitions.

Figure 14 presents the angular momentum as a function of the γ-ray energy for the newly established rotational bands (Bands 1 and 2) in ^{64}Cu and compares these with corresponding data for previously observed highly deformed

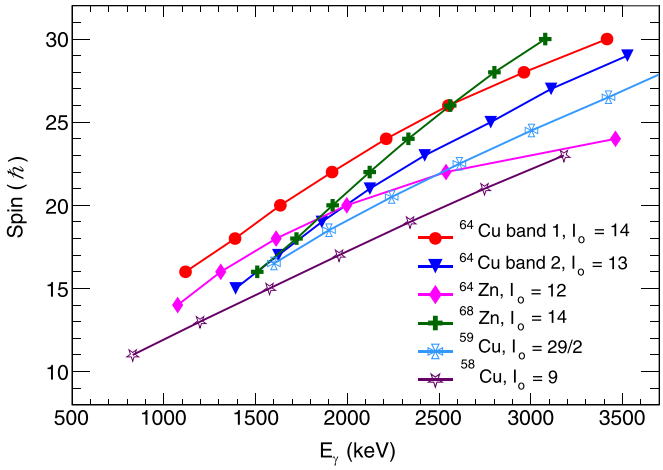

FIG. 14. Angular momentum as a function of transition energy for Band 1 (red circles) and Band 2 (blue triangles) in ^{64}Cu. $I_\circ$ is the bandhead spin. Also shown for comparison are the rotational bands in ^{64}Zn [39], ^{68}Zn [19], ^{59}Cu [15], and ^{58}Cu [14].

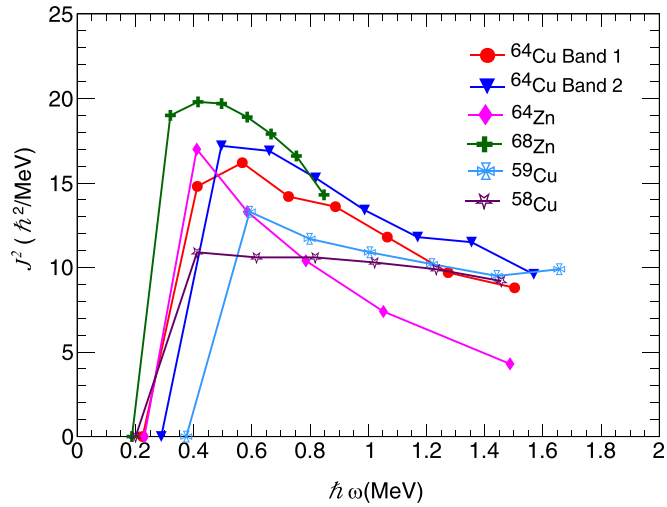

FIG. 15. Experimental dynamic moment of inertia $\mathcal{J}^2$ as a function of the rotational frequency $\hbar\omega$ for Band 1 (red circles) and Band 2 (blue triangles) in ^{64}Cu. Also shown for comparison are the rotational bands in ^{64}Zn [39], ^{68}Zn [19], ^{59}Cu [15], and ^{58}Cu [14].

and superdeformed bands in the neighboring ^{64}Zn [39], ^{63}Ni [8], ^{68}Zn [19], and ^{58,59}Cu nuclei [14,15]. Clearly, the two rotational bands in ^{64}Cu follow a similar trend, and are characterized by very similar slopes, as those in ^{58,59}Cu, suggesting that these ^{64}Cu sequences are associated with intrinsic configurations similar to those of the ^{58,59}Cu superdeformed bands. Similar to the situation in ^{63,65,68}Zn, Band 2 has not been connected to the low-to-medium spin structure of Fig. 3. To investigate the properties of such unlinked bands, it is often useful to consider their dynamic moment of inertia, $\mathcal{J}^{(2)}$, which describes the response of the system as a function of rotational frequency and, hence, can be used to characterize the alignment and collective properties of a deformed nucleus. The $\mathcal{J}^{(2)}$ moments as a function of the rotational frequency $\hbar\omega$ for Bands 1 and 2 in ^{64}Cu are compared in Fig. 15 with those of superdeformed bands in ^{64}Zn, ^{63}Ni, ^{68}Zn, and ^{58,59}Cu. With the increase in rotational frequency, a steady decrease in the $\mathcal{J}^{(2)}$ values is observed in all these cases. It should be noted that this trend is in contrast to the large staggering behavior in $\mathcal{J}^{(2)}$ reported for the ^{60,66}Zn and ^{68}Ge cases (see Fig. 11 in Ref. [11]). As suggested in Ref. [15], this irregularity presumably arises from the simultaneous alignment of $g_{9/2}$ neutrons and protons. For Bands 1 and 2 in ^{64}Cu, however, the steady decrease in $\mathcal{J}^{(2)}$ with $\hbar\omega$, and the similarity with the established superdeformed bands in ^{58,59}Cu provide a strong argument for their classification as superdeformed.

To further understand the nature of these sequences and attempt to determine the associated intrinsic configurations, calculations based on a combination of the constrained covariant density functional theory (CDFT) [40–43] and the quantal particle-rotor model (PRM) [44–50] were performed. This approach has been successfully applied to previous works in this region [9,10]. In the present study, the potential energy surface (PES) of the ground-state configuration obtained by CDFT calculations with the effective interaction PC-PK1 [51] is presented in Fig. 16. In these calculations, the Dirac equation for the nucleons has been solved in a three-dimensional harmonic oscillator basis which, in the present case, includes 12 major oscillator shells. Due to the high-spin nature of these sequences, pairing correlations were neglected. The PES was obtained by constraining the (β, γ) deformation parameters to vary in the intervals $0.0 \leqslant \beta \leqslant 0.6$ and $0^\circ \leqslant \gamma \leqslant 60^\circ$, with step sizes of $\Delta\beta = 0.05$ and $\Delta\gamma = 6^\circ$, respectively. The energies are normalized with respect to the binding energy of the absolute minimum (marked as a circle in Fig. 16). From these calculations, the ground state of ^{64}Cu was found to have a deformation $(\beta, \gamma) = (0.19, 47^\circ)$ with moderate γ

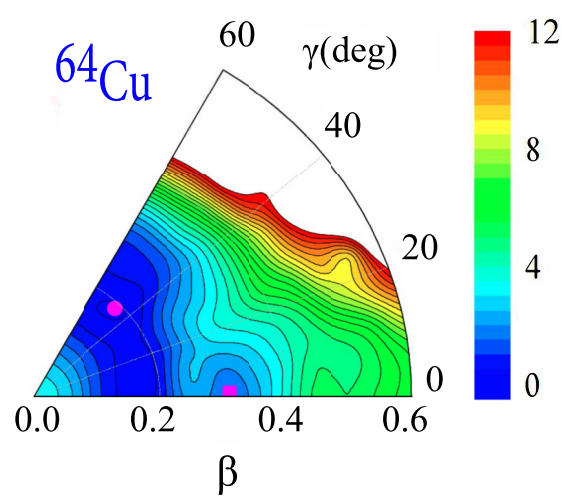

FIG. 16. Potential-energy surface in the $\beta - \gamma$ plane $(0 \leqslant \beta \leqslant 0.6,\ 0^\circ \leqslant \gamma \leqslant 60^\circ)$ for the ground state configuration of ^{64}Cu in CDFT calculations with the PC-PK1 effective interaction. All energies are normalized with respect to that of the absolute minimum (in MeV) indicated by the red circle. The square denotes the local minimum. The energy separation between each contour line is 0.5 MeV.

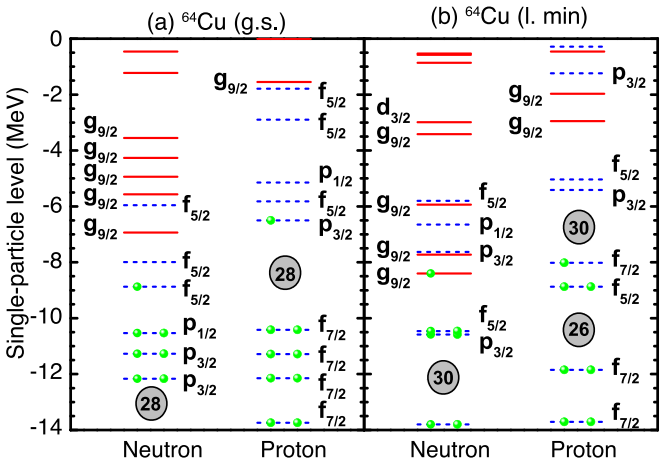

FIG. 17. Single-proton and single-neutron levels near the Fermi surface in ^{64}Cu for the ground state (left) and the states in the local minimum (right).

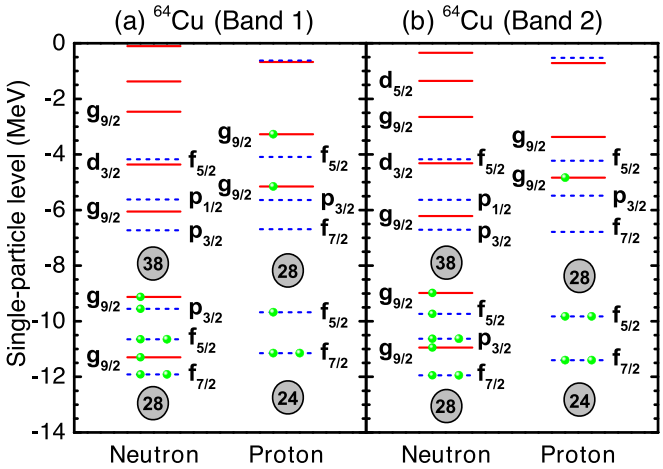

FIG. 18. Same as Fig. 17, but for the configurations of Band 1 (left) and Band 2 (right).

softness. In addition, a local minimum was observed at a prolate deformation of $(\beta, \gamma) = (0.31, 0^\circ)$, which hints towards the existence of superdeformed bands.

Using the adiabatic constrained CDFT calculations, the nucleon occupation of the ground state and of the local minimum was obtained. Figure 17 presents the corresponding single-particle energy levels of protons and neutrons near the Fermi surface for the ground state in ^{64}Cu. The Dirac equation which describes the energetics of the system solved by filling the protons and neutrons into the single-particle energy levels according to their energies from the bottom of the well. For the ground state, it can be seen in Fig. 17 that the conventional magic numbers $Z = 28$ and $N = 28$ remain robust: All shells below $Z = 28$ are fully occupied and the last proton is in the $p_{3/2}$ orbital. Similarly, the last neutron occupies the $f_{5/2}$ orbital. On the other hand, for the lowest level in the prolate minimum associated with a larger deformation, a new sizable gap, in excess of 2 MeV, is seen to be present at $Z = 26, 30$ and $N = 30$. This altered single-particle structure provides the basis for the presence of superdeformed states; such bands in the $A \approx 60$ region are known to be associated with multiple excitations of $\pi f_{7/2}$ and $\nu f_{7/2}$ nucleons into the $\pi g_{9/2}$ and $\nu g_{9/2}$ intruder orbitals near the $Z = N = 30$ superdeformed shell gaps [22].

Configuration-fixed constrained calculations in the CDFT framework were subsequently performed to determine the possible configurations associated with Bands 1 and 2 in ^{64}Cu. For the former a $\pi(1g_{9/2})^2(1f_{5/2})^1 \otimes \nu(1g_{9/2})^2(2p_{3/2})^1$ configuration with deformation $\beta = 0.44$ and $\gamma = 3.3^\circ$ was obtained, while for the latter the $\pi(1g_{9/2})^1 \otimes \nu(1g_{9/2})^2(1f_{5/2})^1$ configuration with $\beta = 0.43$ and $\gamma = 2.2^\circ$ was calculated. On the other hand, a configuration of $\pi(1g_{9/2})^1 \otimes \nu(1g_{9/2})^1$ with deformation of $\beta = 0.28$ and $\gamma = 60^\circ$ accounted for the dipole band (Band 3). It is important note that these configuration were assigned according to the bandhead energy as well as the parity of the observed bands. For example, Band 3 has positive parity. Thus, to determine its configuration and deformation, an inspection of the local minimum and the single-particle energy levels was made. As can be seen in Fig. 17(b), there is already a neutron residing in the $g_{9/2}$ orbital (with positive parity). To obtain a high-j orbital configuration with positive parity, an $f_{7/2}$ (with negative parity) proton is excited to the $g_{9/2}$ orbital (the lowest energy one). Based on this configuration, a configuration-fixed constraint calculation was performed to determine the deformation parameters. To better understand the features of the newly-established superdeformed bands (Band 1 and 2), the single-particle energy levels for protons and neutrons in the vicinity of the Fermi surface are included in Fig. 18. A significant energy gap emerges at $Z = 24$ for both Bands 1 and 2, as can be seen by comparing the single-particle energy levels for the local minimum depicted in Fig. 17(b). Moreover, the neutron $g_{9/2}$ levels exhibit a decrease of approximately 3 MeV. Consequently, the last occupied neutron orbital approaches the substantial $N = 38$ energy gap, thereby enhancing the stability of the superdeformed shape.

Furthermore, PRM calculations [44–50] based on the configurations and deformation parameters from the constrained CDFT calculations were performed in order to study the energy spectra and the electromagnetic properties of the ^{64}Cu sequences. The moments of inertia are those of the irrotational-flow type: $\mathcal{J}_k = \mathcal{J}_0 \sin^2(\gamma - 2k\pi/3)$, with $\mathcal{J}_0$ being adjusted to reproduce the trends seen in the energy spectra of the different bands. The adopted values are $\mathcal{J}_0 = 15$, 13, and 24 $\hbar^2$/MeV for Bands 1, 2, and 3, respectively. For the electromagnetic transitions, the empirical intrinsic quadrupole moment $Q_0 = (3/\sqrt{5\pi})R_0^2 Z\beta$ with $R_0 = 1.2A^{1/3}$ fm was used.

The calculated energy spectra, reduced electric quadrupole transition probabilities, $B(E2)$, and the transition quadrupole moments Q_t are compared with the available data in Fig. 19. Note that for each configuration, the bandhead energy predicted by PRM was shifted in order to compare with the experimental values. The theoretical calculations are able to reproduce the experimental level energies as well as the average Q_t value for Band 1, although the latter is characterized by a large uncertainty.

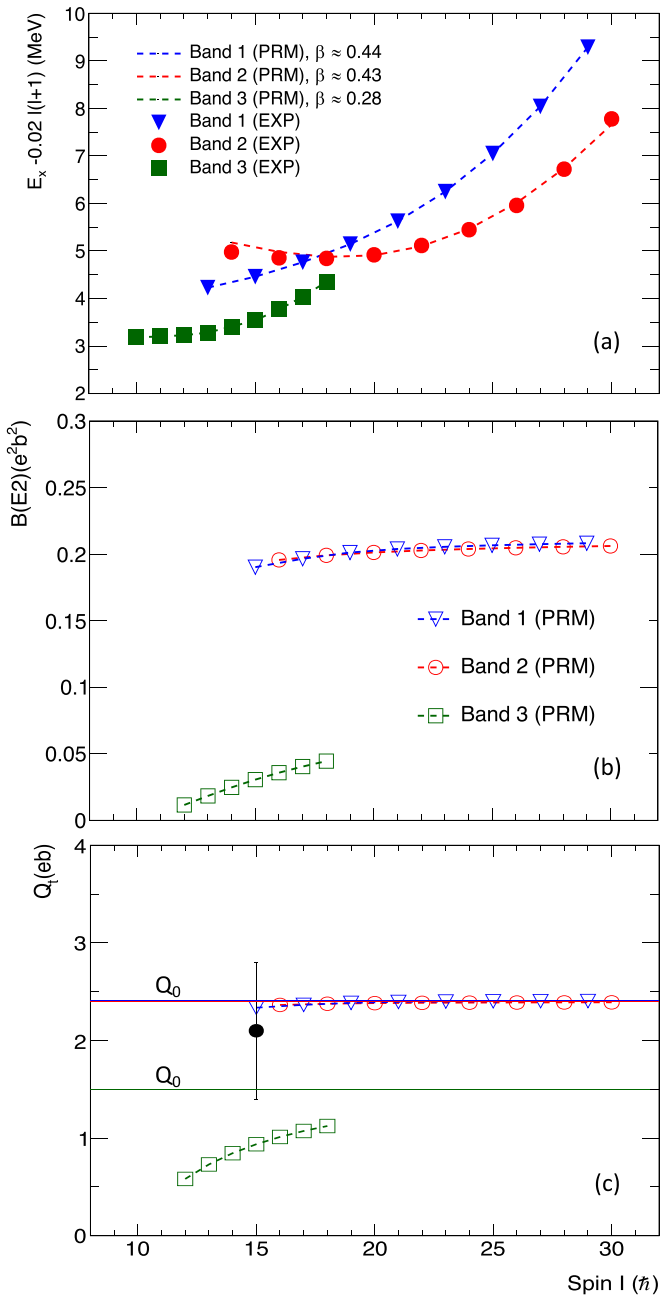

FIG. 19. PRM calculations compared with the available data for ^{64}Cu: (a) energy minus a rotor contribution, (b) computed reduced electric quadrupole transition probabilities $B(E2)$, and (c) calculated transition quadrupole moment Q_t, for Bands 1 and 2 together with the single value for Band 3.

For Bands 1 and 2, the calculated deformations are similar, an observation naturally leading to $B(E2)$ probabilities and Q_t moments of nearly constant value. The Q_t values for both bands were found to be similar to the intrinsic quadrupole moment Q_0. This is due to the deformation being fixed in the PRM calculations along with the Clebsch-Gordon coefficients $\langle I_i K 20 | I_f K\rangle$ ($I_i = I_f + 2$) used to calculate the $B(E2)$ values that have been approximated as a constant value $\sqrt{3/8}$ under the high spin approximation condition $I \gg K$ [52]. This further reveals that the two bands arise from a principal axis rotation with minimal components along the long axis.

For Band 3, with a calculated small oblate deformation, the resulting $B(E2)$ and Q_t values are smaller than those for Bands 1 and 2. In the CDFT framework, the short axis is the symmetry axis. The proton and neutron particles have stable components ($\approx 4.5\hbar$) along the short axis, which corresponds to maximal overlap with the core. With increasing in spin, the core angular momentum gradually increases the component along the long axis. Such an angular momentum coupling forms a principal plane rotational mode with the total angular momentum moving gradually towards the long axis. Correspondingly, Band 3 is a $\Delta I = 1$ rotational sequence, and the $B(E2)$ and Q_t values are seen to increase with spin. Unlike nearby nuclei [3,9,10], where magnetic rotation was suggested for similar dipole bands, the dipole band in ^{64}Cu could not be interpreted in the same framework due to the noticeable crossover transitions in this case.

V. CONCLUSIONS

A detailed study of the level structure of ^{64}Cu was performed by means of the complex multinucleon transfer reaction ^{26}Mg(^{48}Ca, $\alpha p 5 n \gamma$), carried out at beam energies 200% above the Coulomb barrier. The level scheme has been substantially extended up to a spin and parity $I^\pi \approx 29^-$ and an excitation energy of $\approx$27 MeV. Several γ placements as well as multipolarity assignments have been revised from earlier work [30]. While the low-lying level structure was found to be consistent with single-particle/hole excitations, the observation of a dipole band (Band 3) at medium spins, and of two quasirotational bands (Bands 1 and 2) at high spins indicates the onset of collectivity. Bands 1 and 2 were observed in coincidence with the known low-lying structure. However, due to the low intensities involved and the fragmented decay paths, direct linking transitions between Band 2 and the low-spin levels could not be established. Comparisons of these bands with rotational cascades observed in neighboring $A \approx 60$ nuclei suggest the presence of superdeformation at high spin. Calculations carried out within the framework of the adiabatic and configuration-fixed constrained covariant density functional theory and the quantum particle-rotor model suggest configurations for Bands 1 and 2 involving protons and neutrons occupying the $1f_{5/2}$, $2p_{3/2}$, and the intruder $1g_{9/2}$ orbitals. While the dipole band (Band 3) was interpreted as an oblate deformed ($\beta = 0.28$) sequence, Bands 1 and 2 are understood as being associated with a superdeformed shape ($\beta \simeq 0.44$). The observation of superdeformed bands in this nucleus is important because it provides information about the evolution of single-particle excitations as a function of neutron number and angular momentum, as well as about the possible onset of collectivity in the vicinity of $N = 40$. The latter derives in no small measure from the significant role of the $\pi g_{9/2}$ and $\nu g_{9/2}$ intruder orbitals in stabilizing highly-deformed nuclear shapes in the region. However, further data, such as those enabling the extraction of transition probabilities and lifetimes, will be required to provide additional insight into the properties. The present study of ^{64}Cu offers yet another example highlighting the diverse phenomena observed

in the nuclei of the $A \approx 60$ region, and provides an avenue for the investigating the interplay between single-particle and collective excitations.

ACKNOWLEDGMENTS

The authors thank J. P. Greene (ANL) for target preparation and the ATLAS operations staff for the efficient running of the accelerator during the experiment. The authors also gratefully acknowledge contributions from C. J. Lister, B. DiGiovine, T. Baugher, M. Alcorta, C. R. Hoffman, and A. M. Rogers. This material is based upon work supported by the U.S. Department of Energy, Office of Science, Office of Nuclear Physics, under Grants No. DE-SC0023010 (UNC), No. DE-FG02-97ER41041 (UNC), No. DE-FG02-97ER41033 (TUNL), No. DE- FG02-08ER41556, No. DE-SC0020451 (MSU), and No. DE-FG02-94ER40848 (UML), and under Contracts No. DE-AC02-06CH11357 (ANL) and No. DE-AC02-98CH10886 (BNL); by the National Science Foundation under Grant No. PHY-1565546 (MSU); and by the National Natural Science Foundation of China under Grant No. 12205103. This research used the resources of Argonne National Laboratory's ATLAS facility, a DOE Office of Science User Facility.

[1] S. Zhu, A. N. Deacon, S. J. Freeman, R. V. F. Janssens, B. Fornal, M. Honma, F. R. Xu, R. Broda, I. R. Calderin, M. P. Carpenter, P. Chowdhury, F. G. Kondev, W. Królas, T. Lauritsen, S. N. Liddick, C. J. Lister, P. F. Mantica, T. Pawłat, D. Seweryniak, J. F. Smith *et al.*, Phys. Rev. C **74**, 064315 (2006).

[2] H. L. Crawford, R. M. Clark, P. Fallon, A. O. Macchiavelli, T. Baugher, D. Bazin, C. W. Beausang, J. S. Berryman, D. L. Bleuel, C. M. Campbell, M. Cromaz, G. de Angelis, A. Gade, R. O. Hughes, I. Y. Lee, S. M. Lenzi, F. Nowacki, S. Paschalis, M. Petri, A. Poves *et al.*, Phys. Rev. Lett. **110**, 242701 (2013).

[3] D. Steppenbeck, R. V. F. Janssens, S. J. Freeman, M. P. Carpenter, P. Chowdhury, A. N. Deacon, M. Honma, H. Jin, T. Lauritsen, C. J. Lister, J. Meng, J. Peng, D. Seweryniak, J. F. Smith, Y. Sun, S. L. Tabor, B. J. Varley, Y.-C. Yang, S. Q. Zhang, P. W. Zhao, and S. Zhu, Phys. Rev. C **85**, 044316 (2012).

[4] A. N. Deacon, S. J. Freeman, R. V. F. Janssens, M. Honma, M. P. Carpenter, P. Chowdhury, T. Lauritsen, C. J. Lister, D. Seweryniak, J. F. Smith, S. L. Tabor, B. J. Varley, F. R. Xu, and S. Zhu, Phys. Rev. C **76**, 054303 (2007).

[5] N. Hoteling, C. J. Chiara, R. Broda, W. B. Walters, R. V. F. Janssens, M. Hjorth-Jensen, M. P. Carpenter, B. Fornal, A. A. Hecht, W. Królas, T. Lauritsen, T. Pawłat, D. Seweryniak, X. Wang, A. Wöhr, J. Wrzesiński, and S. Zhu, Phys. Rev. C **82**, 044305 (2010).

[6] J. Ljungvall, A. Görgen, A. Obertelli, W. Korten, E. Clément, G. de France, A. Bürger, J.-P. Delaroche, A. Dewald, A. Gadea, L. Gaudefroy, M. Girod, M. Hackstein, J. Libert, D. Mengoni, F. Nowacki, T. Pissulla, A. Poves, F. Recchia, M. Rejmund *et al.*, Phys. Rev. C **81**, 061301(R) (2010).

[7] M. Albers, S. Zhu, A. D. Ayangeakaa, R. V. F. Janssens, J. Gellanki, I. Ragnarsson, M. Alcorta, T. Baugher, P. F. Bertone, M. P. Carpenter, C. J. Chiara, P. Chowdhury, H. M. David, A. N. Deacon, B. DiGiovine, A. Gade, C. R. Hoffman, F. G. Kondev, T. Lauritsen, C. J. Lister *et al.*, Phys. Rev. C **94**, 034301 (2016).

[8] M. Albers, S. Zhu, R. V. F. Janssens, J. Gellanki, I. Ragnarsson, M. Alcorta, T. Baugher, P. F. Bertone, M. P. Carpenter, C. J. Chiara, P. Chowdhury, A. N. Deacon, A. Gade, B. DiGiovine, C. R. Hoffman, F. G. Kondev, T. Lauritsen, C. J. Lister, E. A. McCutchan, D. S. Moerland *et al.*, Phys. Rev. C **88**, 054314 (2013).

[9] A. D. Ayangeakaa, S. Zhu, R. V. F. Janssens, M. P. Carpenter, M. Albers, M. Alcorta, T. Baugher, P. F. Bertone, C. J. Chiara, P. Chowdhury, H. M. David, A. N. Deacon, B. DiGiovine, A. Gade, C. R. Hoffman, F. G. Kondev, T. Lauritsen, C. J. Lister, E. A. McCutchan, D. S. Moerland *et al.*, Phys. Rev. C **91**, 044327 (2015).

[10] N. Sensharma, A. D. Ayangeakaa, R. V. F. Janssens, Q. B. Chen, S. Zhu, M. Alcorta, M. P. Carpenter, E. A. McCutchan, F. G. Kondev, T. Lauritsen, D. Seweryniak, C. R. Hoffman, A. M. Rogers, A. Gade, T. Baugher, and P. Chowdhury, Phys. Rev. C **105**, 044315 (2022).

[11] A. D. Ayangeakaa, N. Sensharma, M. Fulghieri, R. V. F. Janssens, Q. B. Chen, S. Zhu, M. Alcorta, M. P. Carpenter, P. Chowdhury, A. Gade, C. R. Hoffman, F. G. Kondev, T. Lauritsen, E. A. McCutchan, A. M. Rogers, and D. Seweryniak, Phys. Rev. C **105**, 054315 (2022).

[12] D. W. Luo, C. Xu, Y. K. Wang, Z. H. Li, R. A. Bark, S. Q. Zhang, H. Hua, S. Y. Wang, J. Peng, X. Q. Li, H. Y. Wu, X. Wang, C. G. Wu, Q. T. Li, J. Lin, Y. Jin, W. Z. Xu, L. Mu, J. Meng, F. R. Xu *et al.*, Phys. Rev. C **105**, 024305 (2022).

[13] C. E. Svensson, C. Baktash, J. A. Cameron, M. Devlin, J. Eberth, S. Flibotte, D. S. Haslip, D. R. LaFosse, I. Y. Lee, A. O. Macchiavelli, R. W. MacLeod, J. M. Nieminen, S. D. Paul, L. L. Riedinger, D. Rudolph, D. G. Sarantites, H. G. Thomas, J. C. Waddington, W. Weintraub, J. N. Wilson, A. V. Afanasjev, and I. Ragnarsson, Phys. Rev. Lett. **79**, 1233 (1997).

[14] D. Rudolph, C. Baktash, J. Dobaczewski, W. Nazarewicz, W. Satuła, M. J. Brinkman, M. Devlin, H.-Q. Jin, D. R. LaFosse, L. L. Riedinger, D. G. Sarantites, and C.-H. Yu, Phys. Rev. Lett. **80**, 3018 (1998).

[15] C. Andreoiu, D. Rudolph, C. E. Svensson, A. V. Afanasjev, J. Dobaczewski, I. Ragnarsson, C. Baktash, J. Eberth, C. Fahlander, D. S. Haslip, D. R. LaFosse, S. D. Paul, D. G. Sarantites, H. G. Thomas, J. C. Waddington, W. Weintraub, J. N. Wilson, and C.-H. Yu, Phys. Rev. C **62**, 051301(R) (2000).

[16] C. E. Svensson, D. Rudolph, C. Baktash, M. A. Bentley, J. A. Cameron, M. P. Carpenter, M. Devlin, J. Eberth, S. Flibotte, A. Galindo-Uribarri, G. Hackman, D. S. Haslip, R. V. F. Janssens, D. R. LaFosse, T. J. Lampman, I. Y. Lee, F. Lerma, A. O. Macchiavelli, J. M. Nieminen, S. D. Paul, D. C. Radford *et al.*, Phys. Rev. Lett. **82**, 3400 (1999).

[17] C.-H. Yu, C. Baktash, J. Dobaczewski, J. A. Cameron, C. Chitu, M. Devlin, J. Eberth, A. Galindo-Uribarri, D. S. Haslip, D. R. LaFosse, T. J. Lampman, I.-Y. Lee, F. Lerma, A. O. Macchiavelli, S. D. Paul, D. C. Radford, D. Rudolph, D. G. Sarantites, C. E. Svensson, J. C. Waddington, and J. N. Wilson, Phys. Rev. C **60**, 031305(R) (1999).

[18] D. Ward, C. E. Svensson, I. Ragnarsson, C. Baktash, M. A. Bentley, J. A. Cameron, M. P. Carpenter, R. M. Clark, M. Cromaz, M. A. Deleplanque, M. Devlin, R. M. Diamond, P. Fallon, S. Flibotte, A. Galindo-Uribarri, D. S. Haslip, R. V. F. Janssens, T. Lampman, G. J. Lane, I. Y. Lee *et al.*, Phys. Rev. C **63**, 014301 (2000).
[19] M. Devlin, A. V. Afanasjev, R. M. Clark, D. R. LaFosse, I. Y. Lee, F. Lerma, A. O. Macchiavelli, R. W. MacLeod, I. Ragnarsson, P. Ring, D. Rudolph, D. G. Sarantites, and P. G. Thirolf, Phys. Rev. Lett. **82**, 5217 (1999).
[20] A. Afanasjev and I. Ragnarsson, Nucl. Phys. A **628**, 580 (1998).
[21] T. Bengtsson and I. Ragnarsson, Nucl. Phys. A **436**, 14 (1985).
[22] A. V. Afanasjev, I. Ragnarsson, and P. Ring, Phys. Rev. C **59**, 3166 (1999).
[23] J. Bleck, R. Butt, K. Lindenberger, W. Ribbe, and W. Zeitz, Nucl. Phys. A **197**, 620 (1972).
[24] P. Green and D. Sheppard, Nucl. Phys. A **274**, 125 (1976).
[25] U. C. Tsan, M. Agard, J. Bruandet, A. Giorni, and J. Longequeue, Nucl. Phys. A **257**, 413 (1976).
[26] M. Delfini, J. Kopecky, J. De Haas, H. Liou, R. Chrien, and P. Endt, Nucl. Phys. A **404**, 225 (1983).
[27] A. K. Basak, M. A. Basher, A. S. Mondal, M. A. Uddin, S. Bhattacherjee, A. Husain, S. K. Das, M. Haque, and H. M. Sen Gupta, Phys. Rev. C **56**, 1983 (1997).
[28] Y. S. Park and W. W. Daehnick, Phys. Rev. **180**, 1082 (1969).
[29] L. Popescu, T. Adachi, G. P. A. Berg, P. von Brentano, D. Frekers, D. De Frenne, K. Fujita, Y. Fujita, E.-W. Grewe, M. N. Harakeh, K. Hatanaka, E. Jacobs, K. Nakanishi, A. Negret, Y. Sakemi, Y. Shimbara, Y. Shimizu, Y. Tameshige, A. Tamii, M. Uchida, H. J. Wörtche, and M. Yosoi, Phys. Rev. C **79**, 064312 (2009).
[30] S. Samanta, S. Das, R. Bhattacharjee, S. Chatterjee, R. Raut, S. S. Ghugre, A. K. Sinha, U. Garg, Neelam, N. Kumar, P. Jones, M. S. Laskar, F. S. Babra, S. Biswas, S. Saha, P. Singh, and R. Palit, Phys. Rev. C **97**, 014319 (2018).
[31] I.-Y. Lee, Nucl. Phys. A **520**, c641 (1990).
[32] C. N. Davids, B. B. Back, K. Bindra, D. J. Henderson, W. Kutschera, T. Lauritsen, Y. Nagame, P. Sugathan, A. V. Ramayya, and W. B. Walters, Nucl. Instrum. Methods Phys. Res., Sect. B **70**, 358 (1992).
[33] D. C. Radford, Nucl. Instrum. Methods Phys. Res., Sect. A **361**, 297 (1995).
[34] N. Sensharma, Wobbling Motion in Nuclei: Transverse, Longitudinal and Chiral, Ph.D. thesis, University of Notre Dame, 2021 (unpublished).
[35] E. F. Moore, T. Lauritsen, R. V. F. Janssens, T. L. Khoo, D. Ackermann, I. Ahmad, H. Amro, D. Blumenthal, M. P. Carpenter, S. M. Fischer, G. Hackman, D. Nisius, F. Hannachi, A. Lopez-Martens, A. Korichi, S. Asztalos, R. M. Clark, M. A. Deleplanque, R. M. Diamond, P. Fallon *et al.*, Phys. Rev. C **55**, R2150 (1997).
[36] J. F. Ziegler, M. Ziegler, and J. Biersack, Nucl. Instrum. Methods Phys. Res., Sect. B **268**, 1818 (2010).
[37] T. Mizusaki, T. Otsuka, M. Honma, and B. A. Brown, Phys. Scr. **T88**, 107 (2000).
[38] C.-H. Yu, C. Baktash, J. Dobaczewski, J. A. Cameron, M. Devlin, J. Eberth, A. Galindo-Uribarri, D. S. Haslip, D. R. LaFosse, T. J. Lampman, I.-Y. Lee, F. Lerma, A. O. Macchiavelli, S. D. Paul, D. C. Radford, D. Rudolph, D. G. Sarantites, C. E. Svensson, J. C. Waddington, and J. N. Wilson, Phys. Rev. C **62**, 041301(R) (2000).
[39] D. Karlgren, R. M. Clark, I. Ragnarsson, C. E. Svensson, D. Ward, R. Wyss, C. Andreoiu, R. A. E. Austin, M. P. Carpenter, M. Cromaz, M. A. Deleplanque, R. M. Diamond, P. Fallon, A. Görgen, R. V. F. Janssens, T. L. Khoo, F. Kondev, G. J. Lane, T. Lauritsen, I. Y. Lee, A. O. Macchiavelli *et al.*, Phys. Rev. C **69**, 034330 (2004).
[40] J. Meng, J. Peng, S. Q. Zhang, and S.-G. Zhou, Phys. Rev. C **73**, 037303 (2006).
[41] J. Meng, H. Toki, S. Zhou, S. Zhang, W. Long, and L. Geng, Prog. Part. Nucl. Phys. **57**, 470 (2006).
[42] J. Meng, J. Y. Guo, Z. P. Li, H. Z. Liang, W. H. Long, Y. F. Niu, Z. M. Niu, J. M. Yao, Y. Zhang, P. W. Zhao, and S. G. Zhou, Prog. Phys. **31**, 199 (2011).
[43] J. Meng, *Relativistic Density Functional for Nuclear Structure* (World Scientific, Singapore, 2016).
[44] Q. B. Chen, B. F. Lv, C. M. Petrache, and J. Meng, Phys. Lett. B **782**, 744 (2018).
[45] E. Streck, Q. B. Chen, N. Kaiser, and Ulf-G. Meißner, Phys. Rev. C **98**, 044314 (2018).
[46] J. Peng and Q. B. Chen, Phys. Lett. B **793**, 303 (2019).
[47] Q. B. Chen, S. Frauendorf, and C. M. Petrache, Phys. Rev. C **100**, 061301(R) (2019).
[48] Q. B. Chen, S. Frauendorf, N. Kaiser, U.-G. Meißner, and J. Meng, Phys. Lett. B **807**, 135596 (2020).
[49] J. Peng and Q. B. Chen, Phys. Lett. B **806**, 135489 (2020).
[50] Q. B. Chen and S. Frauendorf, Eur. Phys. J. A **58**, 75 (2022).
[51] P. W. Zhao, Z. P. Li, J. M. Yao, and J. Meng, Phys. Rev. C **82**, 054319 (2010).
[52] A. Bohr and B. R. Mottelson, *Nuclear Structure* (Benjamin, New York, 1975), Vol. II.